Journal of Materials Chemistry C

# Grain engineered polar-axis-oriented epitaxial Mn2Mo3O8 films with enhanced magnetic transition temperature

| | |
|---|---|
| Journal: | *Journal of Materials Chemistry C* |
| Manuscript ID | TC-ART-02-2023-000730.R1 |
| Article Type: | Paper |
| Date Submitted by the Author: | 08-May-2023 |
| Complete List of Authors: | Mo, Shishin; The University of Tokyo<br>Katayama, Tsukasa; Hokkaido University, research institute for electronic science<br>Chikamatsu, Akira; Ochanomizu University, Department of Chemistry<br>Hasegawa, Tetsuya; Graduate School of Engineering, Department of Material and Life Science |
| | |

# Grain engineered polar-axis-oriented epitaxial $Mn_2Mo_3O_8$ films with enhanced magnetic transition temperature

Shishin Mo[1], Tsukasa Katayama[2,3*], Akira Chikamatsu[4] and Tetsuya Hasegawa[1]

[1]Department of Chemistry, The University of Tokyo, Bunkyo-ku, Tokyo, 113-0033, Japan

[2]Research Institute for Electronic Science, Hokkaido University, Sapporo, Hokkaido, 001-0020, Japan

[3]JST-PRESTO, Kawaguchi, Saitama 332-0012, Japan

[4]Department of Chemistry, Faculty of Science, Ochanomizu University, 2-1-1 Otsuka, Bunkyo-ku, Tokyo 112-8610, Japan

E-mail: katayama@es.hokudai.ac.jp

## Abstract

$Mn_2Mo_3O_8$ is a layered multiferroic material that exhibits unique properties such as two-dimensional magnetism, room-temperature ferroelectric order, and strong magnetoelectric coupling. However, it has a low magnetic transition temperature ($T_N$) of 41 K. Therefore, in this study, we grain engineered polar-axis-oriented $Mn_2Mo_3O_8$ epitaxial films to enhance the $T_N$. $Mn_2Mo_3O_8$ films were grown on yttria-stabilized zirconia (111) substrates. These films consisted of two types of hexagonal grains (*G*1 and *G*2) that were oriented at an angle of 30° with respect to each other while maintaining the ferroelectric polar axis of the film along the out-of-plane direction. Such a dual grain system is a result of the layered structure of $Mn_2Mo_3O_8$, in which the Mn and Mo layers are alternately stacked along the polar axis. The volume fraction of *G*2 was significantly affected by the film thickness and varied widely in the range 2−48%. Importantly, $T_N$ of the grain engineered $Mn_2Mo_3O_8$ films increased to 163 K with increasing the volume fraction. We speculate that this increase in $T_N$ is due to the formation of a three-dimensional magnetic network at the grain boundaries.

## 1. Introduction

Hexagonal $M_2Mo_3O_8$ (where $M$ = 3d transition metal; see Fig. 1(a)) has recently garnered considerable attention because of its unique electronic properties. It exhibits both the magnetoelectric effect and giant thermal Hall effect, which arise due to the coexistence of ferroelectric and ferromagnetic order [1,2]. $M_2Mo_3O_8$ has a layered structure with $P6_3mc$ symmetry, in which the tetrahedral (*tetra*-) and octahedral (*octa*-) $M$ layers and the Mo trimer layers are stacked alternately along the polar axis ($c$-axis) [3]. The $M_6$ and $Mo_6$ hexagons (green and purple hexagons in Fig. 1(b), respectively) in these layers are oriented at an angle of 30° with respect to each other. Owing to this unique layered structure, $M_2Mo_3O_8$ exhibits a wide variety of magnetic properties depending on the choice of $M$, namely: ferrimagnetism for $M$ = Mn, antiferromagnetism for $M$ = Fe and Co, and canted antiferromagnetism for $M$ = Ni [2,4]. The magnetic properties of $M_2Mo_3O_8$ can be controlled by manipulating the external magnetic field, electric field, and temperature [1,2,5].

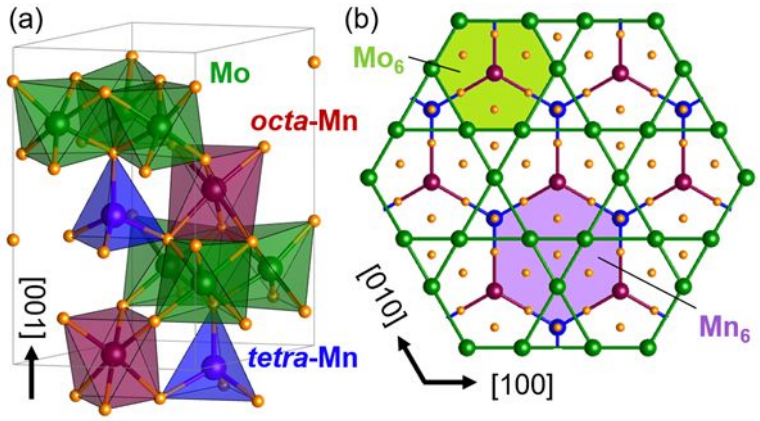


**Figure 1.** $Mn_2Mo_3O_8$ (or MMO): (a) crystal structure and (b) top view.

In addition to powders and bulk single crystals [4,6-11], epitaxial $M_2Mo_3O_8$ films for $M$ = Mn have been prepared on $Al_2O_3$ (001) substrates using pulsed laser deposition (PLD) [12]. Tensile-strained $Mn_2Mo_3O_8$ (hereafter MMO) films exhibit a larger spontaneous magnetization and polarization and a higher Néel temperature ($T_N$) than bulk single crystals [4,12], demonstrating that

strain engineering is a promising way to modify the ferroic properties of MMO films. MMO films exhibit a $T_N$ of 108 K; however, this value is considerably low and needs to be improved. Grain engineering has been shown to be effective in improving the magnetic properties of materials. For example, the coercivity of hard magnetic materials is sensitive to the grain size [13]. In addition, grain engineering can be used to modulate the magnetic phase of materials. For instance, the emergence of a ferromagnetic phase has been reported at the grain boundaries in antiferromagnetic $TbMnO_3$ [14].

For MMO films synthesized on $Al_2O_3$ (001) substrates, there is only one type of grain lattices, in which the *a*- and *c*-axes of MMO are aligned along the [120] and [001] directions of $Al_2O_3$, respectively [12]. This is because the crystal orientation is determined by the degree of lattice matching between the $Mo_6$ hexagons in the Mo layer of MMO and $Al_6$ hexagons in the (001) plane of $Al_2O_3$ [12]. However, if a substrate exhibits ionic bonding with the $Mn_6$ hexagons in addition to the $Mo_6$ hexagons during film deposition, then grains with two different orientations are formed while maintaining the polar-axis of the film along the out-of-plane direction. Thus, grain engineering can be used to modulate the magnetic properties of MMO films. In this study, we fabricated polar-axis-oriented epitaxial MMO films on yttria-stabilized zirconia (YSZ; (111)) substrates. These films were composed of two types of grains (*G*1 and *G*2) that were aligned at an angle of 30° with respect to each other along the in-plane direction. Two types of grains were obtained because the lattice mismatch between the substrate and $Mo_6$ hexagons was similar to that between the substrate and $Mn_6$ hexagons. The volume fraction ($V_f$) of *G*2 was controlled by manipulating the film thickness such that $V_f$ was obtained to be in the range 2−48%. $T_N$ increased with increasing $V_f$ and reached a maximum of 163 K, which is approximately four times higher than that of bulk MMO crystal (41 K).

## 2. Experiments

MMO thin films were fabricated on YSZ (111) substrates using PLD. A ceramic pellet composed of $Mn_2Mo_3O_8$ was used as the target material. The deposition was performed at 850 °C and

$10^{-4}$ Torr in an $Ar/H_2$ (97:3) atmosphere. A KrF laser ($\lambda$ = 248 nm) with a frequency of 5 Hz and energy in the range 4–5 J $cm^{-2}$ $shot^{-1}$ was used for the deposition. Notably, YSZ (111) substrates are useful for fabricating hexagonal oxide epitaxial films and are readily available in 1-inch sizes. The crystal structure and film thickness were determined using X-ray diffraction (XRD) and X-ray reflectometry, respectively, using Cu-$K\alpha_1$ radiation (Bruker, D8 DISCOVER). The surface morphology was studied using atomic force microscopy (AFM; Hitachi AFM5000II) and imaged using Gwyddion [15]. The magnetization was evaluated using a superconducting quantum interference device (SQUID) magnetometer (Quantum Design MPMS XL), and the crystal structure was visualized using VESTA [16]. The dielectric properties have not been investigated because the YSZ substrate is an insulator. However, it may be possible to investigate ferroelectric properties by using indium tin oxide as the bottom electrode layer, which has the same crystal structure as YSZ.

## 3. Results and discussion

Figure 2(a) shows the out-of-plane $2\theta$–$\theta$ XRD patterns of the MMO films deposited on YSZ (111) substrates. Only the 00*l* diffraction peaks were observed, indicating that the films were oriented along the polar axis. The lengths of the *c*-axis of the films with thickness 35 and 100 nm were 10.21 and 10.19 Å, respectively, which were slightly shorter than that of bulk MMO (10.24 Å [6]) but longer than that of the MMO films deposited on $Al_2O_3$ (001) substrates (10.17 Å [12]). On the other hand, the length of the *a*-axis, which was evaluated from the 112 diffraction peak, was longer than that of bulk MMO, indicating that the films were subjected to tensile straining (Table S1).

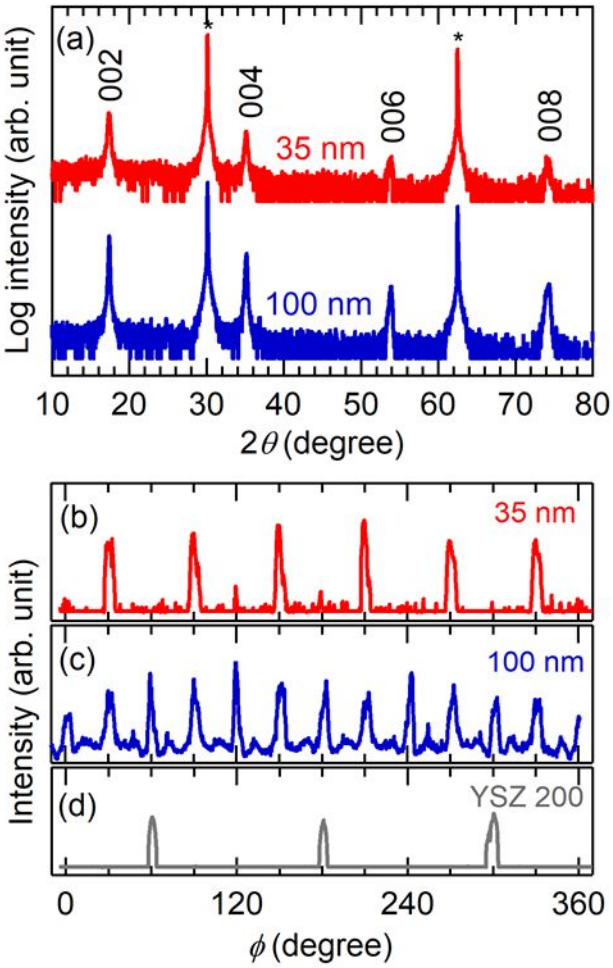


**Figure 2.** (a) Out-of-plane $2\theta$–$\theta$ XRD patterns of MMO films of thickness 35 and 100 nm. $\phi$-scan profile of the {112} diffraction peak of MMO films of thickness: (b) 35 nm and (c) 100 nm on YSZ (111) substrates. (d) $\phi$-scan of the {200} diffraction peak of YSZ.

The in-plane orientations of the films were investigated using $\phi$-scan measurements. Since the out-of-plane $2\theta$–$\theta$ XRD measurements confirmed that the films are *c*-axis oriented (Fig. 2(a)), we can expect how much the (112) plane of the MMO is tilted from the surface normal axis; i.e., $2\theta$ and $\omega$ values for observing the 112 diffraction peak of MMO are determined. After setting the $2\theta$ and $\omega$ values, $\phi$-scans were measured by rotating the films around the surface normal axis, where $\phi$ is in-plane rotation angle. Figures 2(b) and (c) show the $\phi$-scan profiles of the {112} diffraction peak of

MMO films of thickness 35 and 100 nm formed on a YSZ substrate, respectively. In case of the MMO film of thickness 35 nm, intense peaks were observed at an interval of 60°. Note that the $\phi$ values were shifted by 30° compared to the {200} peaks of YSZ (see Fig. 2(d)). This indicates that the [100] axis of MMO (hereafter $[100]_{MMO}$) was parallel to the [11-2] axis of YSZ (hereafter $[11\text{-}2]_{YSZ}$). Weak diffraction peaks were also observed between two intense peaks. This implies that the MMO film of thickness 35 nm contained a second type of crystal domain with $[100]_{MMO} \parallel [1\text{-}10]_{YSZ}$ (where $\parallel$ denotes "parallel to"). Hereafter, the two crystal domains with $[100]_{MMO} \parallel [11\text{-}2]_{YSZ}$ and $[100]_{MMO} \parallel [1\text{-}10]_{YSZ}$ are referred to as *G*1 and *G*2, respectively. The value of $V_f$ of *G*2 was determined from the intensity ratio of the 112 diffraction peaks of MMOs between *G*1 and *G*2. Although MMOs in *G*1 and *G*2 have different orientations, the crystal structure of the MMOs is the same. Thus, the ratio of the intensity of the 112 diffraction peak is proportional to the volume fraction. From the intensity ratio of the peaks, $V_f$ of *G*2 in the MMO film of thickness 35 nm was determined to be only 2%. However, when the film thickness was increased from 35 to 100 nm, the {112} peaks became significantly more intense (Fig. 2(c)) and $V_f$ of *G*2 increased to 44%. By contrast, MMO films formed on an $Al_2O_3$ substrate consisted of only one type of crystal domain with $[100]_{MMO} \parallel [120]_{Al2O3}$ [12].

The Mo and Mn layers in MMO are stacked alternately along the *c*-axis, as shown in Fig. 1(a). When projected onto the *ab*-plane, one of the sides of the $Mo_6$ hexagon (green) is parallel to $[100]_{MMO}$, whereas one of the sides of the (purple) hexagon composed of three *octa*-$Mn_6$ and three *tetra*-$Mn_6$ layers is parallel to $[120]_{MMO}$, as shown in Fig. 1(b). The atoms of YSZ also form a hexagon ($Zr_3O_3$; gray hexagon in Fig. 3), and one of its sides is parallel to $[11\text{-}2]_{YSZ}$. In *G*1, the $Mo_6$ hexagons have the same orientation as the $Zr_3O_3$ hexagons; moreover, approximately three $Mo_6$ hexagons ($3\sqrt{3}a_{MMO}$ / 2 = 15.1 Å) match with four $Zr_3O_3$ hexagons ($2\sqrt{2}a_{YSZ}$ = 14.5 Å). Conversely, in *G*2 (Fig. 3(b)), two Mn(VI) hexagons ($2a_{MMO}$ = 11.6 Å) match with three $Zr_3O_3$ hexagons ($3\sqrt{2}a_{YSZ}$ / 2 = 10.9 Å). Therefore, the lattice mismatch between the MMO film and YSZ substrate is 4.1 and 6.4% in *G*1 and *G*2, respectively. For a film thickness of 35 nm, $V_f$ of *G*1 was significantly higher than that of *G*2,

probably because of the lower lattice mismatch in *G*1.

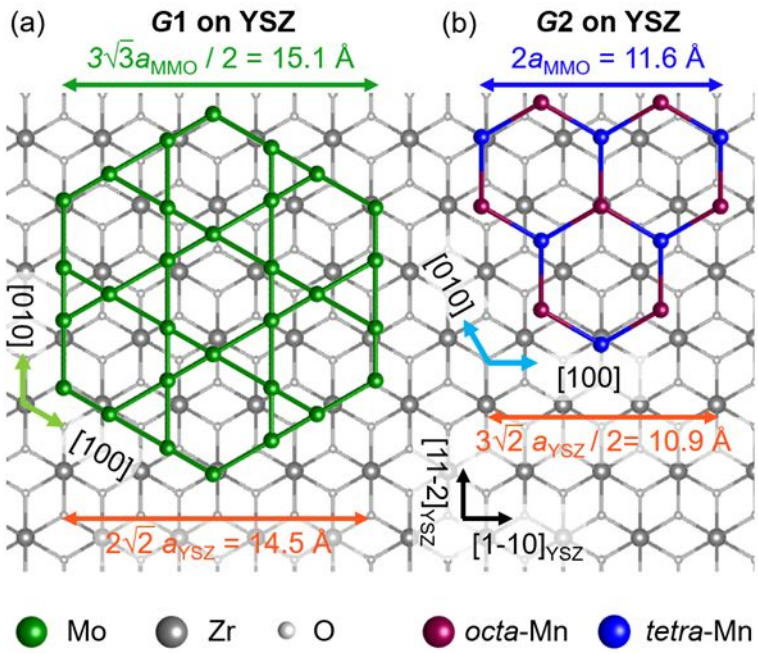


**Figure 3.** Lattice mismatch between the MMO film and YSZ substrate in (a) *G*1 and (b) *G*2.

To investigate the effect of film thickness on $V_f$ of *G*2, we fabricated MMO films of thickness in the range of 15−100 nm on YSZ substrates. All the films exhibited 00*l* diffraction peaks in their out-of-plane XRD patterns (Fig. S1). The diffraction peaks for the film of thickness 15 nm were significantly broader than those of the films with a larger thickness, indicating low crystallinity. Figure 4 and S2 show the AFM images of the MMO films formed on YSZ. The film of thickness 15 nm exhibited small islands with an average area of 0.3 μm$^2$. These islands did not have a clear hexagonal shape. For the film of thickness 20 nm, both hexagonal and non-hexagonal islands were observed, where hexagonal islands tend to have higher thickness. One of the sides of the hexagonal islands was parallel to $[11\text{-}2]_{YSZ}$. The film of thickness 35 nm exhibited mostly hexagonal islands with one of the sides parallel to $[11\text{-}2]_{YSZ}$ (and hence to $[100]_{MMO}$). Conversely, the films of thickness 52 and 100 nm exhibited two types of hexagonal islands—one with sides parallel to $[11\text{-}2]_{YSZ}$ and the other with sides

parallel to $[1\text{-}10]_{YSZ}$, corresponding to *G*1 and *G*2, respectively.

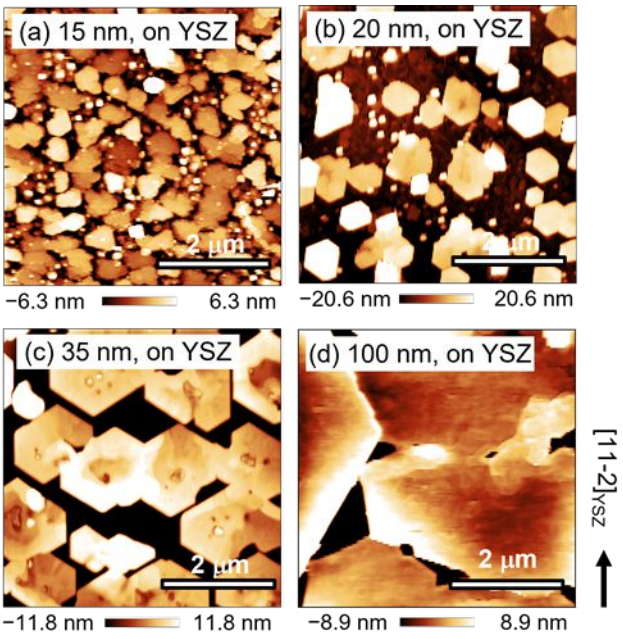


**Figure 4**. AFM images of the MMO films on YSZ substrates with thickness (a) 15, (b) 20, (c) 35, and (d) 100 nm.

Figure 5(a) shows $V_f$ of *G*2 as a function of the film thickness. The value of $V_f$ decreased from 9 to 2% as the film thickness increased from 15 to 35 nm; however, with a further increase in film thickness from 35 to 52 nm, the value of $V_f$ increased from 2 to 48%. Figure 5(b) shows the dependence of the average size of the islands observed in the AFM images on the film thickness. The average size of the islands increased monotonically from 0.3 to >25 $\mu m^2$ as the film thickness increased from 15 to 100 nm. The XRD and AFM results reveal a strong correlation between the size of the islands and $V_f$ of *G*2. As the film thickness increased from 35 to 52 nm, the size of the islands increased by a factor of ~20, indicating that several islands coalesced to form one big island via the migration of atoms. In addition, approximately half of the *G*1 grains rotated by 30° and converted to *G*2 grains. The rotation of the grains suggests that the stacking fault energy of MMO is small probably due to its layered

structure. Notably, such island coalescence often creates defects, including Frank faults, leading to the formation of dislocations and/or cracks in the film [17-19].

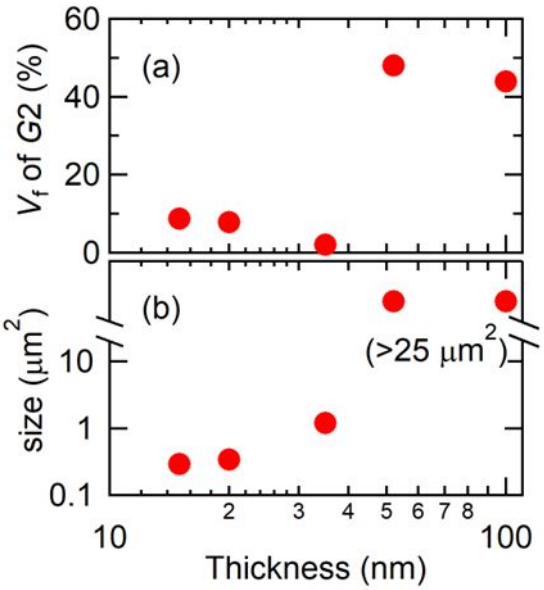


**Figure 5.** (a) $V_f$ of $G2$ and (b) average size of the islands in the AFM image as a function of the thickness of the MMO films on YSZ substrates.

The large variation in $V_f$ (of $G2$) with film thickness can be explained using AFM measurements, the results of which can be summarized as follows: (1) island growth was observed in the MMO films; (2) the size of the islands increased with film thickness; and (3) the hexagonal islands were larger in size compared to the non-hexagonal islands for a film thickness of 20 nm. These results indicate that the MMO crystals grew around the seed crystals scattered on the substrate. Moreover, the growth rate of the $G1$ seed crystals was higher than that of the $G2$ seed crystals, resulting in the low $V_f$ of $G2$ for film thickness less than 35 nm. The higher growth rate of the $G1$ seed crystals is probably due to the lower lattice mismatch between the MMO film and substrate in $G1$ (4.1%) than in $G2$ (6.4%), as shown in Fig. 3. However, when the film thickness is larger than 52 nm, the adjacent islands overlap and a migration of atoms occurs as the islands coalesce. In this case, thermodynamic stability becomes

the dominant factor for determining $V_f$ rather than the growth rate of the seed crystals; i.e., the Gibbs free energy, given by $\Delta G = \Delta H - T\Delta S$, attains a minimum, where $\Delta H$ and $\Delta S$ are the differences in enthalpy and entropy, respectively, between *G*1 and *G*2. Because the shape and size of the *G*1 and *G*2 grains are similar (Fig. 4(d)), $\Delta H$ is mainly determined by the difference in the stabilization energy between *G*1 and *G*2 owing to the epitaxial strain in the substrate. The $\Delta H$ value increases with increasing $V_f$; i.e., from an enthalpy standpoint, a decrease in $V_f$ towards zero leads to more stability. On the other hand, since entropy increases as the number of states increases, $-T\Delta S$ decreases as $V_f$ approaches 50% and/or grain size decreases. Considering that $V_f$ of *G*2 is 48 and 44% for a film thickness of 52 and 100 nm, respectively, the substrate-induced stabilization energy for *G*1 is higher than that for *G*2. However, the effect of the enthalpy term is less than that of the entropy term. If the grain size decreases in the equilibrium state, the number of possible states increases, making the entropy term more important and leading to an increase in $V_f$. However, for the MMO films with a thickness below 35 nm, despite having smaller grain sizes, $V_f$ remained small compared to the MMO films with a thickness above 52 nm. This indicates that thin film growth at low thicknesses is not in equilibrium but rather in a non-equilibrium state.

We also investigated the magnetic properties of the MMO films. The inset in Fig. 6 shows the in-plane magnetization as a function of the magnetic field ($M-H$ curves) for the MMO films of thickness 35 and 100 nm on YSZ substrates at 2 K. Magnetic hysteresis loops were clearly observed, indicating the presence of ferrimagnetic order in these films. Such ferrimagnetic behavior has also been observed in MMO films on $Al_2O_3$ substrates [12]. The spontaneous magnetization for the MMO films of thickness 35 and 100 nm on YSZ was 0.32 and 0.26 $\mu_B$/f.u., respectively, which is similar to that for MMO films on $Al_2O_3$ (0.35 $\mu_B$/f.u.) [12]. Figure 6 also shows the $M-T$ curves of the MMO films on YSZ. $T_N$ was estimated using the Kouvel–Fisher method. $T_N$ of the MMO films of thickness 100 nm and 35 nm on the YSZ substrate was 163 K and 122 K, respectively; whereas, $T_N$ of the MMO films on the $Al_2O_3$ substrate and bulk MMO crystals was 108 K [12] and 41 K [4], respectively. Table

S1 shows the lattice constants of bulk MMO crystal and MMO films deposited on $Al_2O_3$ and YSZ substrates. The *c*-axis length of the films shrinks compared to that of the bulk, while the *a*-axis length tends to elongate. This tensile strain is likely to have a significant effect on $T_N$. In particular, the shrinkage of the *c*-axis length is expected to enhance the magnetic interactions along the *c*-axis direction. However, as for the thin films, a strong correlation between lattice constant and $T_N$ was not observed. Thus, in addition to the influence of substrate-induced strain, there is an effect of grain engineering. One possible explanation for the higher $T_N$ in the MMO film of thickness 100 nm on the YSZ substrate is that the magnetic interaction between the Mn ions is modified at the dislocations in the film and/or grain boundaries between *G*1 and *G*2. This significantly affects the bulk magnetic properties owing to the formation of an additional magnetic network. For example, in antiferromagnetic $TbMnO_3$, a ferromagnetic phase has been observed at the boundaries of the domain walls [14]. In addition, the magnetic phase of $GdBaCo_2O_{5.5}$ has been reported to change from antiferromagnetic to ferrimagnetic (more stable) due to the existence of domain boundaries [20]. MMO has a layered structure in which magnetic Mn plane and non-magnetic Mo plane are alternately stacked along the *c*-axis (Fig. 1(a)). Since Mn ions have strong superexchange interaction mediated by one oxygen ion in the *ab*-plane, the magnetic interaction in the *ab*-plane is predicted to be approximately 2.5 times stronger than that along the *c*-axis [21]. Such a two-dimensional magnetic network generally results in a lower magnetic transition temperature compared to that in a three-dimensional magnetic network [22,23]. Thus, a higher $T_N$ can be obtained if the dislocations in the film and/or grain boundaries between *G*1 and *G*2 forms a three-dimensional magnetic network. Furthermore, in thin films and nanoparticles, the grain size is known to be an important factor for governing the magnetic transition temperature; hence, manipulating the grain size can also lead to a higher $T_N$ [24].

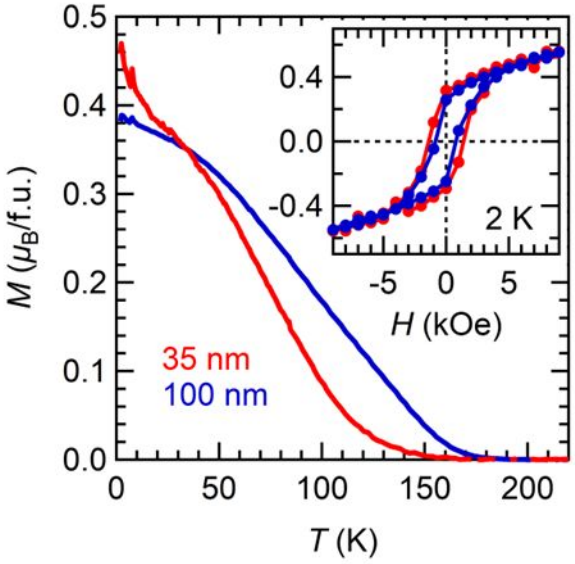


**Figure 6.** In-plane $M-T$ curves for MMO films of thickness 35 and 100 nm on YSZ substrates. The inset shows the corresponding $M-H$ curves at 2 K.

## 4. Conclusion

We fabricated MMO films of different thicknesses on YSZ (111) substrates. XRD and AFM measurements revealed that the films consisted of two types of in-plane grains such that the *a*-axis of MMO in these grains was parallel to: (i) $[11\text{-}2]_{YSZ}$ and (ii) $[1\text{-}10]_{YSZ}$, which we refer to as *G*1 and *G*2, respectively. The value of $V_f$ of *G*2 was low (2−9%) when the film thickness was less than 35 nm but increased to approximately 50% when the film thickness was greater than 50 nm. The MMO film of thickness 100 nm exhibited ferrimagnetic properties with a $T_N$ of 163 K, which is significantly higher than that of bulk MMO (41 K). This increase in $T_N$ is probably derived from the formation of a three-dimensional magnetic network at the grain boundaries. We believe that the grain engineering technique developed in this study can be applied specifically to layered hexagonal oxide materials, some of which exhibit excellent magnetic properties. For example, hexagonal $BaFe_{12}O_{19}$ with layered structure accounts for 50% of the weight ratio of the industrialized hard magnetic materials, due to its low cost,

high quality, and atmospheric stability [25]. In the actual applications, grain engineering is important to achieve high coercivity. However, unlike bulk materials, the development of grain engineering for thin films has been lagging behind, although thin-film $BaFe_{12}O_{19}$ has a high potential for applications in memory, sensors, and isolators. Our findings would have the potential to contribute to the development of magnetic materials for such applications.

## Acknowledgments

This work was supported by JST PRESTO (JPMJPR21Q3), JSPS KAKENHI (20H02614) and Kao Foundation for Arts and Sciences.

## Supporting information

See supporting information for details of the XRD and AFM results.

## References

[1] T. Kurumaji, S. Ishiwata and Y. Tokura, Phys. Rev. B, 2017, 95, 045142.

[2] Y. S. Tang, S. M. Wang, L. Lin, C. Li, S. H. Zheng, C. F. Li, J. H. Zhang, Z. B. Yan, X. P. Jiang and J.-M. Liu, Phys. Rev. B, 2019, 100, 134112.

[3] P. Strobel and Y. Le Page, J. Cryst. Growth, 1983, 61, 329–338.

[4] S. P. McAlister and P. Strobel, J. Magn. Magn. Mater., 1983, 30, 340–348.

[5] Y. Wang, G. L. Pascut, B. Gao, T. A. Tyson, K. Haule, V. Kiryukhin and S.-W. Cheong, Sci. Rep., 2015, 5, 12268.

[6] H. Abe, A. Sato, N. Tsujii, T. Furubayashi and M. Shimoda, J. Solid State Chem., 2010, 183, 379–384.

[7] S. P. McAlister and P. Strobel, J. Magn. Magn. Mater., 1983, 30, 340–348.

[8] Y. Sun, X. Hu, W. Luo and Y. Huang, J. Mater. Chem., 2011, 21, 17229–17235.

[9] B. Das, M. V. Reddy, C. Krishnamoorthi, S. Tripathy, R. Mahendiran, G. V. S. Rao and B. V. R. Chowdari, Electrochim. Acta, 2009, 54, 3360–3373.

[10] B. Lippold, J. Herrmann, W. Reichelt and H. Oppermann, Phys. status solidi, 1990, 121, K91–K94.

[11] L. Zhang, K. Shen, W. He, Y. Liu, L. Yin and S. Guo, J. Phys. Chem. Solids, 2018, 121, 71–77.

[12] S. Mo, T. Katayama, A. Chikamatsu, M. Kitamura, K. Horiba, H. Kumigashira and T. Hasegawa, Chem. Mater., 2021, 33, 7713–7718.

[13] G. Herzer, IEEE Trans. Mag., 1990, 26, 1397–1402.

[14] S. Farokhipoor, C. Magén, S. Venkatesan, J. Íñiguez, C. J. M. Daumont, D. Rubi, E. Snoeck, M. Mostovoy, C. de Graaf, A. Müller, M. Döblinger, C. Scheu and B. Noheda, Nature, 2014, 515, 379–383.

[15] D. Nečas and P. Klapetek, Open Phys., 2012, 10, 181–188.

[16] K. Momma and F. Izumi, J. Appl. Crystallogr., 2011, 44, 1272–1276.

[17] L. H. Kuo, L. Salamanca-Riba, B. J. Wu, G. M. Haugen, J. M. DePuydt, G. Hofler, H. Cheng, J. Vacuum Sci. Technol. B 1995, 13, 1694–1704.

[18] V. Narayanan, K. Lorenz, W. Kim and S. Mahajan, Appl. Phys. Lett. 2001, 78, 1544–1546.

[19] X. H. Wu, L. M. Brown, D. Kapolnek, S. Keller, B. Keller, S. P. DenBaars, J. S. Speck, J. Appl. Phys. 1996, 80, 3228–3237.

[20] T. Katayama, A. Chikamatsu, Y. Zhang, S. Yasui, H. Wadati and T. Hasegawa, Chem. Mater., 2021, 33, 5675–5680.

[21] D. Szaller, K. Szász, S. Bordács, J. Viirok, T. Rõõm, U. Nagel, A. Shuvaev, L. Weymann, A. Pimenov, A. A. Tsirlin, A. Jesche, L. Prodan, V. Tsurkan and I. Kézsmárki, Phys. Rev. B, 2020, 102, 144410.

[22] C. Gong, L. Li, Z. Li, H. Ji, A. Stern, Y. Xia, T. Cao, W. Bao, C. Wang, Y. Wang, Z. Q. Qiu, R. J. Cava, S. G. Louie, J. Xia and X. Zhang, Nature, 2017, 546, 265–269.

[23] B. Huang, G. Clark, E. Navarro-Moratalla, D. R. Klein, R. Cheng, K. L. Seyler, Di. Zhong, E. Schmidgall, M. A. McGuire, D. H. Cobden, W. Yao, D. Xiao, P. Jarillo-Herrero and X. Xu, Nature, 2017, 546, 270–273.

[24] X. G. Zheng, C. N. Xu, K. Nishikubo, K. Nishiyama, W. Higemoto, W. J. Moon, E. Tanaka and E. S. Otabe, Phys. Rev. B - Condens. Matter Mater. Phys., 2005, 72, 014464.

[25] R. C. Pullar, Prog. Mater. Sci. 2012, 57, 1191–1334.